 doi:10.20944/preprints202101.0157.v1

Evaluation of coating thickness using lift-off insensitivity of eddy current sensor

Xiaobai Meng [1,*], Mingyang Lu [2,*], Wuliang Yin [2], Abdeldjalil Bennecer [1], and Katherine J Kirk [1]

[1] Faculty of Art, Science and Technology, University of Northampton, Northampton, NN1 5PH, United Kingdom; xiaobai.meng@northampton.ac.uk (X.M.); abdeldjalil.bennecer@northampton.ac.uk (A.B.); katherine.kirk@northampton.ac.uk (K.J.K.)

[2] School of Electrical and Electronic Engineering, University of Manchester, Sackville Street Building, Manchester, M13 9PL, United Kingdom; mingyang.lu@manchester.ac.uk (M.L.); wuliang.yin@manchester.ac.uk (W.Y.)

* Correspondence: xiaobai.meng@northampton.ac.uk (X.M.); mingyang.lu@manchester.ac.uk (M.L.)

Abstract: Defect detection in ferromagnetic substrates is often hampered by non-magnetic coating thickness variation when using conventional eddy current testing technique. The lift-off distance between the sample and the sensor is one of the main obstacles for the thickness measurement of non-magnetic coatings on ferromagnetic substrates when using the eddy current testing technique. Based on the eddy current thin-skin effect and the lift-off insensitive inductance (LII), a simplified iterative algorithm is proposed for reducing the lift-off variation effect using a multi-frequency sensor. Compared to the previous techniques on compensating the lift-off error (e.g., the lift-off point of intersection) while retrieving the thickness, the simplified inductance algorithms avoid the computation burden of integration, which are used as embedded algorithms for the online retrieval of lift-offs via each frequency channel. The LII is determined by the dimension and geometry of the sensor, thus eliminating the need for empirical calibration. The method is validated by means of experimental measurements of the inductance of coatings with different materials and thicknesses on ferrous substrates (dual-phase alloy). The error of the calculated coating thickness has been controlled to within 3 % for an extended lift-off range of up to 10 mm.

Keywords: Multi-frequency eddy current; lift-off inversion; coating thickness; non-destructive testing; multi-layer conductor.

1. Introduction

Coatings serve as protective barriers for substrate materials in industrial applications. In order to investigate their characteristics, various non-destructive techniques, chiefly eddy current (EC) sensing, have been used to directly measure the thickness of coating on a conductive substrate in a non-contact manner [1-4].

Diverse methods using EC sensors have been proposed for the measurement of coating thickness. Kim et al reported a non-contact and on-line method using a dual EC sensor setup to reduce the measurement error of film coatings [5]. An EC testing-based method has been applied to measure the impedance of the conductive substrate and determine the coating thickness [6]. Considering the ferrous substrate, Yang and Tai have used the swept-frequency eddy-current (SFEC) for the determination of the substrate permeability, which serve as the input for subsequent measurements of conductivity and thickness of coatings using the pulsed eddy current (PEC) method [7-11]. Other methods including the dual-frequency EC sensing technique [12], swept-frequency [13-15] and single-frequency [16] eddy current sensing for the thickness measurement of non-metallic coatings, error compensations on the thickness of conductive coatings [17], reconstruction of multi-layer electromagnetic parameters [18,19], numerical models [20], and alternative strategies on

 doi:10.20944/preprints202101.0157.v1

monitoring the coatings [21]. The proposed techniques can cope with small lift-off variations of up to 6 mm for either magnetic or non-magnetic materials.

In practical measurements, the sensitivity of the EC signal is frequency-dependent and varies with different values of material and geometric properties (e.g., thickness) [22], which then affects the reliability and accuracy of the defect evaluation. Therefore, it is necessary to analyse the characteristics of sensor-sample using signals obtained from different frequencies using multi-frequency eddy current (MEC) testing. Compared to the PEC, the MEC has better signal-to-noise ratio (SNR) particularly under high working frequencies [23]). By using multiple frequency channels [24] and curve-matching functions (e.g., polynomials), online real-time monitoring of parameters can be achieved. However, like other EC techniques, MEC can be significantly affected by coating variations that manifest in the lift-off distance between the sensor and test piece. Previously, to address the lift-off issue, a time-domain feature, the lift-off point of intersection has been used for the measurement of coating thickness based on the PEC [25].

For the MEC, previous works have been proposed to reduce the error (caused by the lift-off distance variation) to derive important parameters such as the thickness (single layer), magnetic permeability, and electrical conductivity of samples [25-39]. The methods involve novel sensor structure (e.g., triple-coil eddy current sensor system), compensation algorithms, and frequency features (e.g., revised/compensated peak frequency for non-magnetic or zero-crossing frequency for ferromagnetic materials). [40-46]. However, few methods have directly derived the lift-off distance. Besides, previous scenarios on reducing the error of lift-offs merely apply for a smaller range of lift-offs (mostly up to 6 mm). Moreover, previous methods merely apply to the single-layer conductive structures. For the dual-layer plates, properties of substrates (including the thickness, electrical conductivity, and magnetic permeability) significantly affect the measured signals (voltage, impedance, or inductance). Thus, alternative features are required to retrieve the thickness of coatings on ferromagnetic substrates using the MEC testing.

In this paper, a simplified iterative algorithm is proposed for the computation of inductance value under high working frequencies to cancel the lift-off effect. The simplified algorithm is based on the eddy-current thin-skin feature. That is, the inductance measured by the sensor is shown to be independent of the test piece (including the coating thickness) under high working frequencies. The lift-off is retrieved based on the proposed eddy-current thin-skin feature. Furthermore, it has been found that the inductance becomes insensitive to the lift-off at a certain value (termed as the lift-off insensitive inductance). The lift-off insensitive inductance is a quiescent value, which is shown to be material independent. Therefore, based on the retrieved lift-off and frequency of the lift-off insensitive inductance (LII) for different coatings, the thickness of coatings has been retrieved using an iterative method. Compared with our previous work on the thickness retrieval [52], an alternative sensor design with two sensing pairs is used, which has considered the sensitivities of sensing pairs with different lift-off on the retrieval of both lift-off and thickness retrieval (The lower sensing coil is sensitive to the coating thickness, while the upper one is sensitive to the lift-off spacing between the coil and test piece). Besides, the previous research work [52] focusing on the thickness retrieval of single-layer non-ferromagnetic materials. In this paper, the influence of ferromagnetic substrate is considered for the thickness retrieval of non-ferromagnetic coatings. The ferromagnetic substrate is permeable (and even can be magnetized under large driving current or restrained eddy current under high-frequency skin effect) and thus affect the measured inductance and its sensitivities to different parameters [22] under different lift-offs and frequencies). Moreover, compared to [52], instead of retrieving the thickness under a random working frequency, a lift-off insensitive inductance feature is found in this paper (where the inductance is significantly less sensitive to the lift-off for a sensor dependent inductance). The coating thickness is retrieved by referring to the corresponding frequency (merely determined by the test piece and significantly sensitive to the lift-off) of the lift-off insensitive inductance (merely determined by the sensor and independent of the test piece) on the

Preprints (www.preprints.org) | NOT PEER-REVIEWED | Posted: 8 January 2021 doi:10.20944/preprints202101.0157.v1

multi-frequency inductance spectrum. The measurement is based on the triple-stacked coil [22] sensor setup, but different dimensions and strategies of signal processing. The previous technique on the lift-off retrieval is based on the iterative method on conventional analytical model, whereas the proposed technique is using the thin-skin regime via simplified model (which only needs single frequency for the lift-off retrieval, and applies for the online measurement). Experiments on the inductance measurement of a ferrous dual-phase substrate with non-magnetic coatings of different materials and thicknesses have been carried out. The thickness of different coatings has been retrieved based on the retrieved lift-off and frequency of LII (termed as the lift-off insensitive frequency) with an error of less than 3 % for lift-offs up to 10 mm.

2. Analytical algorithms

For eddy current sensing coils above the coated conductors (e.g., Fig. 1), several parameters (including coating thickness c, lift-off spacing l_0 between sensor and test piece, electrical conductivities of coatings and substrate, and relative permeability of ferromagnetic substrate) affect the measured inductance (L_1 and L_2 from transmitting-receiving 1 ($T-R_1$) and transmitting-receiving 2 ($T-R_2$) sensing pairs). The aim is to find the function of retrieving the coating thickness c (i.e., $c = F(L_1, L_2)$), where the function F needs to be calibrated.

To address the unwanted lift-off effect, the lift-off spacing is retrieved from the inductance L_2 ($T-R_2$ sensing pair) via a simplified function. Then, a lift-off insensitive inductance feature is proposed to retrieve the coating thickness c from the retrieved lift-off via $T-R_1$ sensing pair.

2.1. Original formulas – Inductance of coils above a dual-layer conductive structure

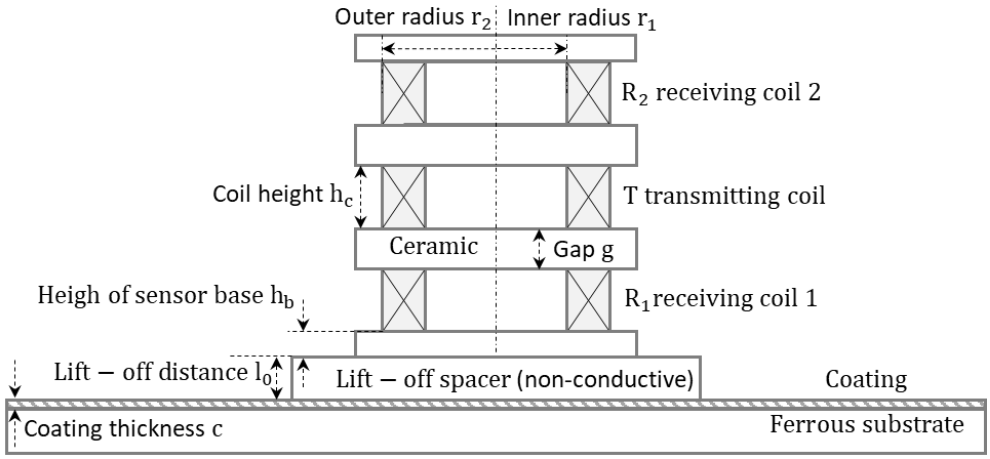

Figure 1. Circular coils above a dual-layer structure.

In Fig. 1, the eddy current sensor consists of three identical circular coils. To fully receive the reflected magnetic flux from the specimen, two receiving coils are aligned co-axially with the transmitting coil.

Based on the Green's functions, Dodd-Deeds formulas [47] have been massively applied for the analytical computation of mutual inductance between conductive samples and different sensor structures [40-42, 48, 49]. As shown in Fig. 1, the inductance change (values due to the sample minus those for the sensor in the free space) for the transmitting-receiving 1 ($T-R_1$) and transmitting-receiving 2 ($T-R_2$) are given as following expressions.

$$L_1(c,f) = K\int_0^\infty M_1\,\varphi d\alpha \tag{1}$$

$$L_2(c,f) = K\int_0^\infty M_2\,\varphi d\alpha \tag{2}$$

Preprints (www.preprints.org) | NOT PEER-REVIEWED | Posted: 8 January 2021 doi:10.20944/preprints202101.0157.v1

In (1) and (2), L_1 and L_2 vary with the frequency f of the exciting current and coating thickness c. α is the variable of integration, which is related to the wavenumber of the incident transverse electric (TE) planar electromagnetic wave [47, 50-52]. φ is the material-dependent phase term for the mutual inductance., K is defined as followings.

$$K = \frac{\pi\mu_0 N^2 (r_2 + r_1)}{2h_c^2 (r_2 - r_1)^2} \tag{3}$$

For the cross-sectional circular coil, h_c is the coil height. N is the number of turns. r_1 and r_2 are the inner and outer radii of coil. μ_0 denotes the vacuum magnetic permeability. M_1 and M_2 mainly control the magnitude of integrand for the mutual inductance in (1) and (2) respectively, which are merely determined by the dimension and structure of sensors.

$$M_1 = \frac{P^2(\alpha)}{\alpha^6} e^{-\alpha(h_c+g+2h_b+2l_0)} (e^{-\alpha h_c} - 1)^2 \tag{4}$$

$$M_2 = \frac{P^2(\alpha)}{\alpha^6} e^{-\alpha(3h_c+3g+2h_b+2l_0)} (e^{-\alpha h_c} - 1)^2 \tag{5}$$

In (4) and (5),

$$P(\alpha) = \int_{\alpha r_1}^{\alpha r_2} \tau J_1(\tau) d\tau \tag{6}$$

J_1 is the first-order Bessel function of the first kind. τ is the variable of integration. h_b is the height of the sensor base. l_0 is the lift-off distance between the sensor and test piece. g is the gap between coils.

By integrating the magnitude (M_1 or M_2) and phase term φ over the entire wavenumber domain, the whole contributions of inductance from TE planar electromagnetic waves can be derived.

As shown in Fig. 1, for the dual-layer conductive structure, the phase of the integrand in (1) and (2) is expressed as.

$$\varphi = \mathrm{Re}\left(\frac{(\alpha+\beta_1)(\beta_1-\beta_2) - (\alpha-\beta_1)(\beta_1+\beta_2)e^{2\alpha_1 c}}{(\alpha-\beta_1)(\beta_1-\beta_2) + (\alpha+\beta_1)(\beta_1+\beta_2)e^{2\alpha_1 c}} \right) \tag{7}$$

In (7),

$$\alpha_1 = \sqrt{\alpha^2 + j2\pi\sigma_1\mu_1\mu_0 f} \tag{8}$$

$$\beta_1 = \frac{\sqrt{\alpha^2 + j2\pi\sigma_1\mu_1\mu_0 f}}{\mu_1} \tag{9}$$

$$\beta_2 = \frac{\sqrt{\alpha^2 + j2\pi\sigma_2\mu_2\mu_0 f}}{\mu_2} \tag{10}$$

f is the working frequency of the current flowing in the transmitter coil. μ_1 and μ_2 are the relative permeability of top and bottom layers respectively (i.e., the coating and substrate in Fig. 1). σ_1 and σ_2 are the electrical conductivity of the coating and substrate. α_1 and β_1 are related to the wavenumber of the TE planar electromagnetic wave within coatings. β_2 is related to the wavenumber of the TE planar electromagnetic wave within substrates [47, 50], considering the effect of material inhomogeneities of different layers.

2.2. Proposed method – Eddy-current thin-skin algorithms for the retrieval of lift-off

For the case of the non-magnetic coating on the ferromagnetic substrate, φ in (7) becomes,

$$\varphi = \mathrm{Re}\left(\frac{(\alpha+\alpha_1)(\mu_2\alpha_1-\alpha_2) - (\alpha-\alpha_1)(\mu_2\alpha_1+\alpha_2)e^{2\alpha_1 c}}{(\alpha-\alpha_1)(\mu_2\alpha_1-\alpha_2) + (\alpha+\alpha_1)(\mu_2\alpha_1+\alpha_2)e^{2\alpha_1 c}} \right) \tag{11}$$

In (11),

Preprints (www.preprints.org) | NOT PEER-REVIEWED | Posted: 8 January 2021 doi:10.20944/preprints202101.0157.v1

$$\alpha_2 = \sqrt{\alpha^2 + j2\pi\sigma_2\mu_2\mu_0 f} \tag{12}$$

α_2 is related to the wavenumber of the TE planar electromagnetic wave within substrates.

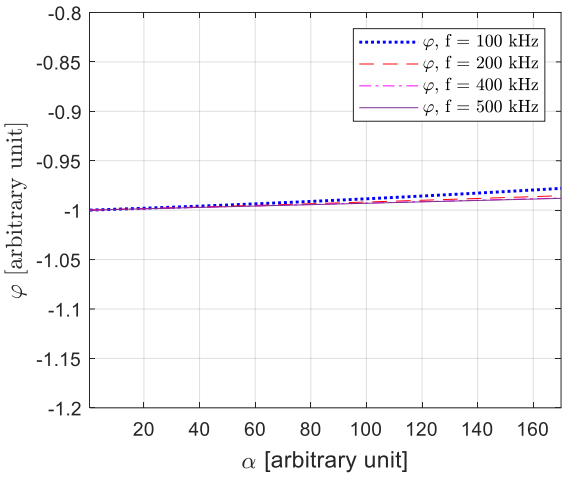

(a)

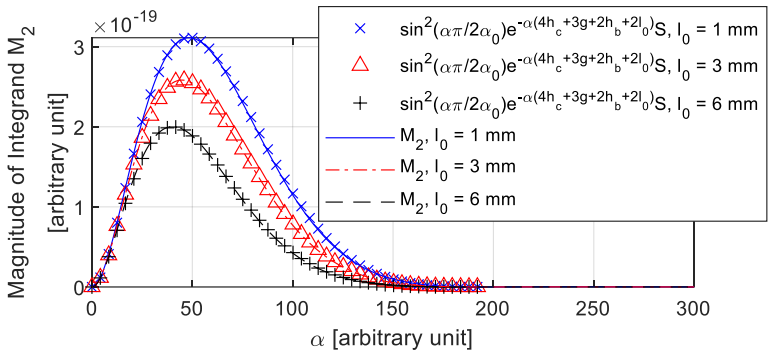

(b)

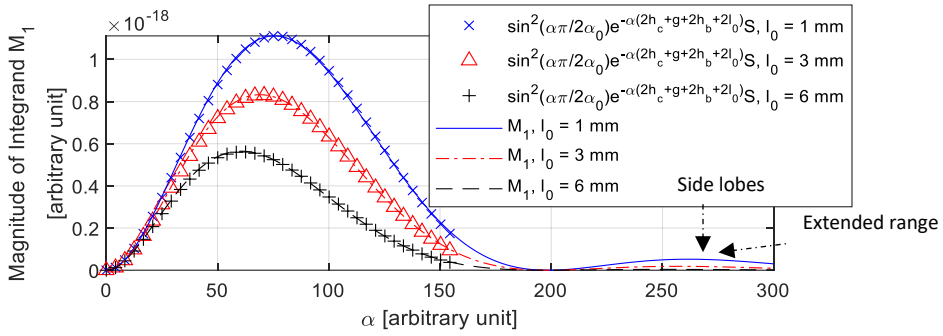

(c)

Figure 2. (a) Phase of the integrand in (1) and (2) (b) Matched function for the magnitude of the integrand in (2) (c) Side lobes occur in the magnitude of the integrand in (1); the range of α extends.

In Fig. 2, it is found that under relatively high working frequencies (normally over 100 kHz for most of non-magnetic metals), the phase φ changes very slowly compared to the magnitude part (In Fig. 2 b). Thus, φ can be approximated as a constant.

$$\varphi = -1 \tag{13}$$

It is found that a larger lift-off of receiver coil could avoid side lobes in the magnitude of the integrand (M_1 in Fig. 2 c). Moreover, the effective range of α in M_2 is found to be narrower than in M_1,

Preprints (www.preprints.org) | NOT PEER-REVIEWED | Posted: 8 January 2021 doi:10.20944/preprints202101.0157.v1

which results in a better high-frequency approximation in (13). Therefore, the lift-off is obtained from $T-R_2$ sensing pair.

Since the J_1 (the first-order Bessel function of the first kind) is similar to the sinusoidal function with a decay factor. In Fig. 2 b, for the magnitude part of integrand in (2), it is found that the Bessel series $\frac{P^2(\alpha)}{\alpha^6}e^{\alpha h_c}(e^{-\alpha h_c}-1)^2$ can be well fitted by a sinusoidal function $\sin^2\left(\frac{\alpha\pi}{2\alpha_0}\right)$. α_0 is a sensor-dependent factor, which is determined by parameters h_c, r_1, and r_2. Hence, M_2 can be expressed as,

$$M_2 = Se^{-\alpha(4h_c+3g+2h_b+2l_0)}\sin^2\left(\frac{\alpha\pi}{2\alpha_0}\right) \tag{14}$$

In (14), S is a normalisation factor between the Bessel function (for variable α) and the sinusoidal function (for variable α). S is derived from the ratio between two functions at the peak of sinusoidal function when α arrives at $\alpha=\alpha_0$.

$$S = \frac{P^2(\alpha_0)}{\alpha_0^6}e^{\alpha_0 h_c}(e^{-\alpha_0 h_c}-1)^2 \tag{15}$$

It can be seen in (15) that S is determined by the sensor-dependent constant α_0 instead of the wavenumber valuable α.

Substituting (14) into (2), the high-frequency inductance becomes,

$$L_2(c,f) = -K\int_0^{2\alpha_0} Se^{-\alpha(4h_c+3g+2h_b+2l_0)}\sin^2\left(\frac{\alpha\pi}{2\alpha_0}\right)d\alpha \tag{16}$$

Assume $(x = 4h_c+3g+2h_b+2l_0)$, evaluating the integral yields,

$$L_2(c,f) = -\frac{\pi^2 KS(1-e^{-2\alpha_0 x})}{2x(\alpha_0^2x^2+\pi^2)} \tag{17}$$

In (17), $e^{-2\alpha_0 x} \ll 1$ as $2\alpha_0 x \gg 1$. Thus,

$$2x(\alpha_0^2x^2+\pi^2)L_2(c,f)+\pi^2KS=0 \tag{18}$$

Assume the solution of x in the function (18) is x_0, the lift-off is,

$$l_0 = \frac{x_0-3g}{2}-2h_c-h_b \tag{19}$$

2.3. Proposed method - Iterative algorithms based on a lift-off insensitive inductance for the retrieval of coating thickness

As receiver 1 (R_1) is closer and more sensitive to the coating, the signal of $T-R_1$ sensing pair is used for the retrieval of coating thickness. As can be observed from Fig. 3 a, swept-frequency inductance curves with different lift-offs nearly intersect at an inflection point. It is found that the inductance of the intersected point is independent of the test piece (including the thickness of coatings). The inductance and frequency of the intersected point are termed as the lift-off insensitive inductance (LII) and lift-off insensitive frequency (LIF) respectively. Thus, the thickness of coatings can be retrieved by referring to the LIF feature. In practical measurement, inductance curves may intersect at multiple cluster points. Consequently, LII is the least-squares value of the inductance for different lift-offs under LIF. Moreover, LIF is selected when the inductance deviation of different lift-offs under a single frequency reaches its lowest value.

Preprints (www.preprints.org) | NOT PEER-REVIEWED | Posted: 8 January 2021 doi:10.20944/preprints202101.0157.v1

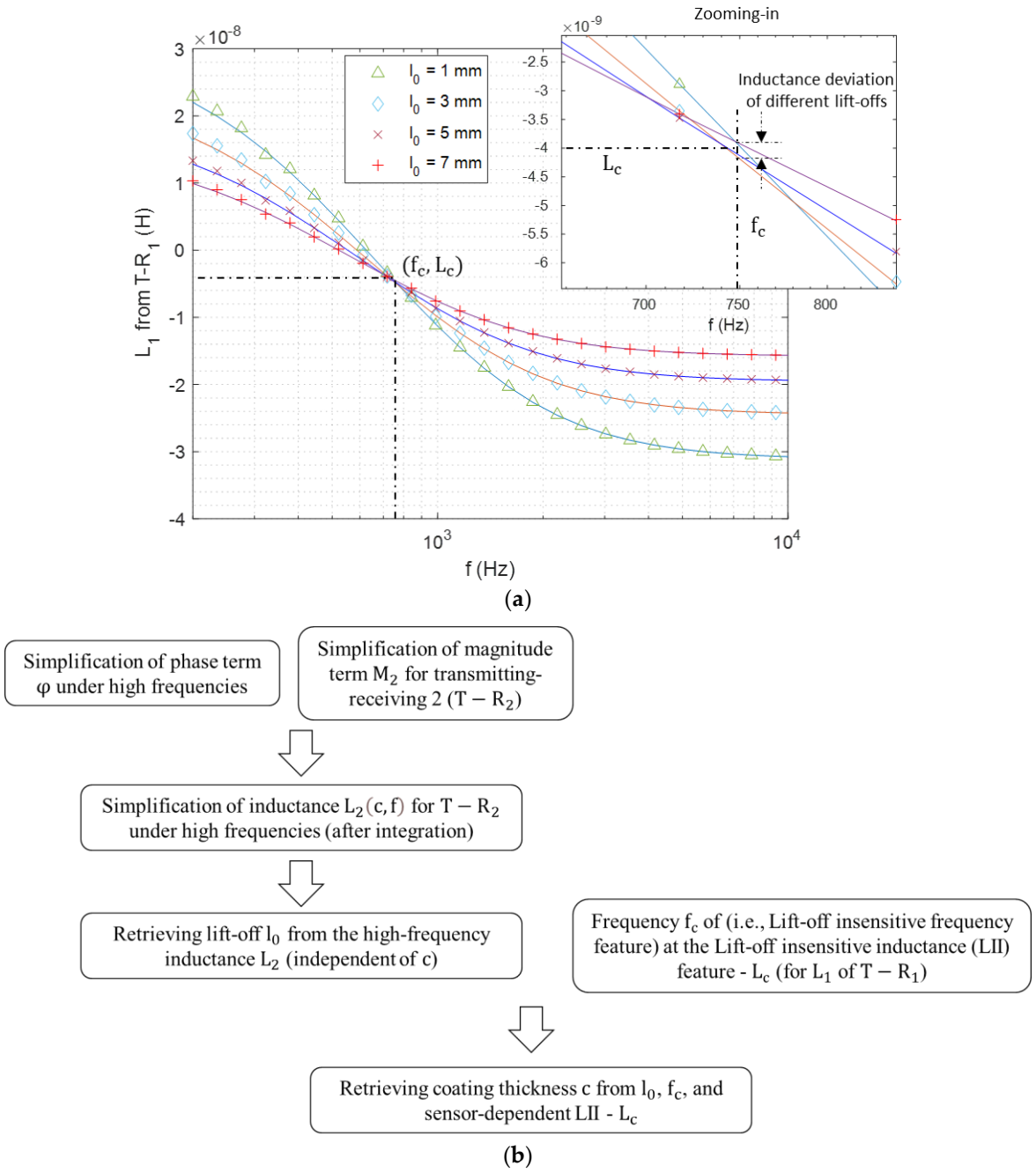

(**a**)

(**b**)

Figure 3. (a) Swept-frequency inductance curves of different lift-off distances (solid lines – analytical results via equation 1, markers – experimental results) for T − R_1 above the substrate (DP 1000) with aluminium coating of 0.3 mm (Table 1). (b) Algorithmic flowchart

Table 1. Properties of samples.

	Electrical conductivity (MS/m)	**Relative magnetic permeability**	**Thickness (mm)**
Substrate – DP 1000	3.81	122	4.0
Coating – Brass	15.9	1	0.1,0.3,0.5
Coating – Aluminium	36.9	1	0.1,0.3,0.5

Preprints (www.preprints.org) | NOT PEER-REVIEWED | Posted: 8 January 2021 doi:10.20944/preprints202101.0157.v1

Referring to the signal processing method based on the modified Newton-Raphson method [22], the thickness of coatings can be restored in an iterative manner.

$$c = \Delta c + c_r \tag{20}$$

c_r is the reference coating thickness. The increment term Δc is defined as,

$$\Delta c = J^{-1}(L_1(c_r, f_c, l_0) - L_c) \tag{21}$$

$L_1(c_r, f_c, l_0)$ denotes the inductance expressed in equation (1) for the reference coating thickness (c_r), LIF (f_c) and derived lift-off l_0. L_c is the sensor dependent LII. J is the Jacobian matrix, which denotes the inductance sensitivity with respect to c_r.

$$J = \frac{L_1(c_r, f_c, l_0) - L_1(c_r + \rho c_r, f_c, l_0)}{\rho c} \tag{22}$$

In (22), ρ is a residual value (ρ is assigned as 0.01 here).

Fig. 3 b depicts the algorithmic flow of strategies on retrieving the coating thickness from the measured inductance of eddy current sensing coils.

3. Experiments

To investigate the inverse algorithm from (18) to (22), experiments have been conducted on the inductance measurement of the triple-coil sensor above the ferrite-austenite dual-phase (DP) 1000 substrate with coatings of different non-magnetic materials and thicknesses (Table 1). Different thicknesses of coatings are achieved by stacking a series of thin foils. Since the eddy current is parallel to the coating, the induced eddy current is mainly parallel to the coating layers. Consequently, impedance interferences between foils are neglectable.

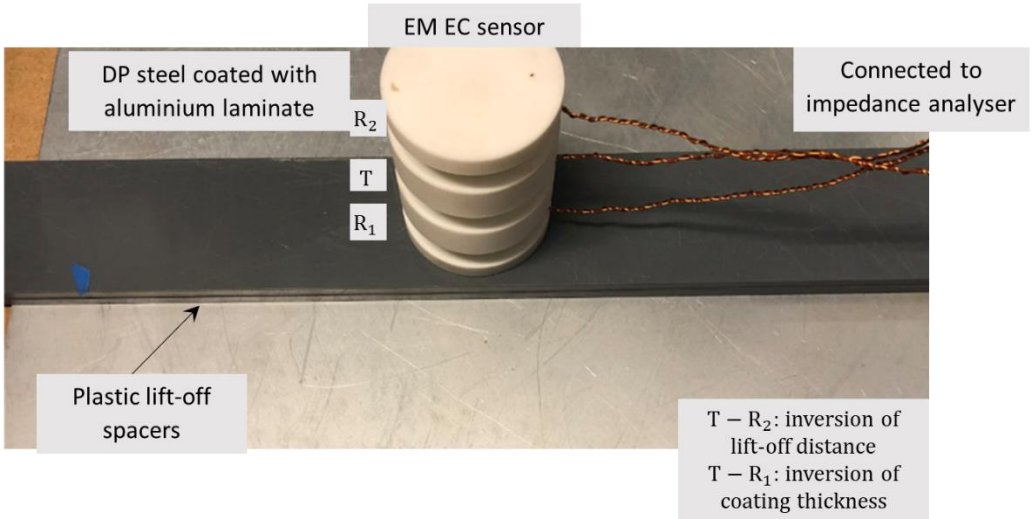

(**a**)

Preprints (www.preprints.org) | NOT PEER-REVIEWED | Posted: 8 January 2021 doi:10.20944/preprints202101.0157.v1

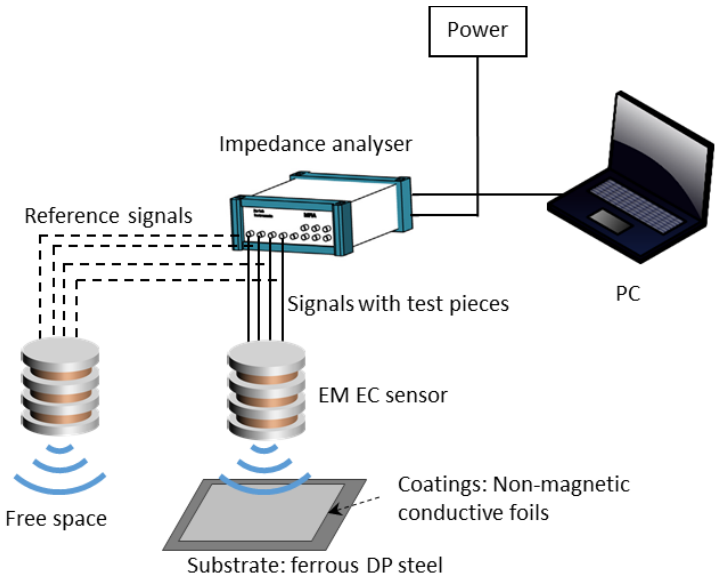

Figure 4. Experimental setup (a) sensor placed on the test piece (b) sensor connected to the measurement system (impedance analyser).

Table 2. Properties of sensor structures and excitation signals.

Parameters	
Inner radius r_1 (mm)	19.0
Outer radius r_2 (mm)	19.6
Turns N	20
Gap g (mm)	10.0
Coil height h_c (mm)	6.0
Heigh of sensor base h_b (mm)	4.0
Lift-offs l_0 (mm)	1.0:1.0:10.0
Working frequency	200 Hz ~ 500 kHz
Lift-off insensitive inductance L_c (H)	-4×10^{-9}

As shown in Table 2 and Fig. 4, the frame of eddy-current sensor is designed as a ceramic structure, which contains three co-axial circular buckets. Three identical coil windings are wound seamlessly in the ceramic slot. In the measurement, the eddy-current sensor is placed on layers of plastic spacers to mock the lift-off effect.

In Fig. 4, the sensor is connected to the impedance analyser for the measurement of swept-frequency inductance for both free space and above the test piece. The inductance change is the value due to the sample minus that for the sensor in the free space. Considering the SNR and ambient effects (including the resonant/proximity/parasitic effect, and Barkhausen noise effect – where the permeability of ferrous substrate becomes frequency dependent) under low and high working frequencies respectively, the frequency range is set from 200 Hz to 500 kHz.

Preprints (www.preprints.org) | NOT PEER-REVIEWED | Posted: 8 January 2021 doi:10.20944/preprints202101.0157.v1

4. Result and analysis

4.1. Retrieval of lift-off distance

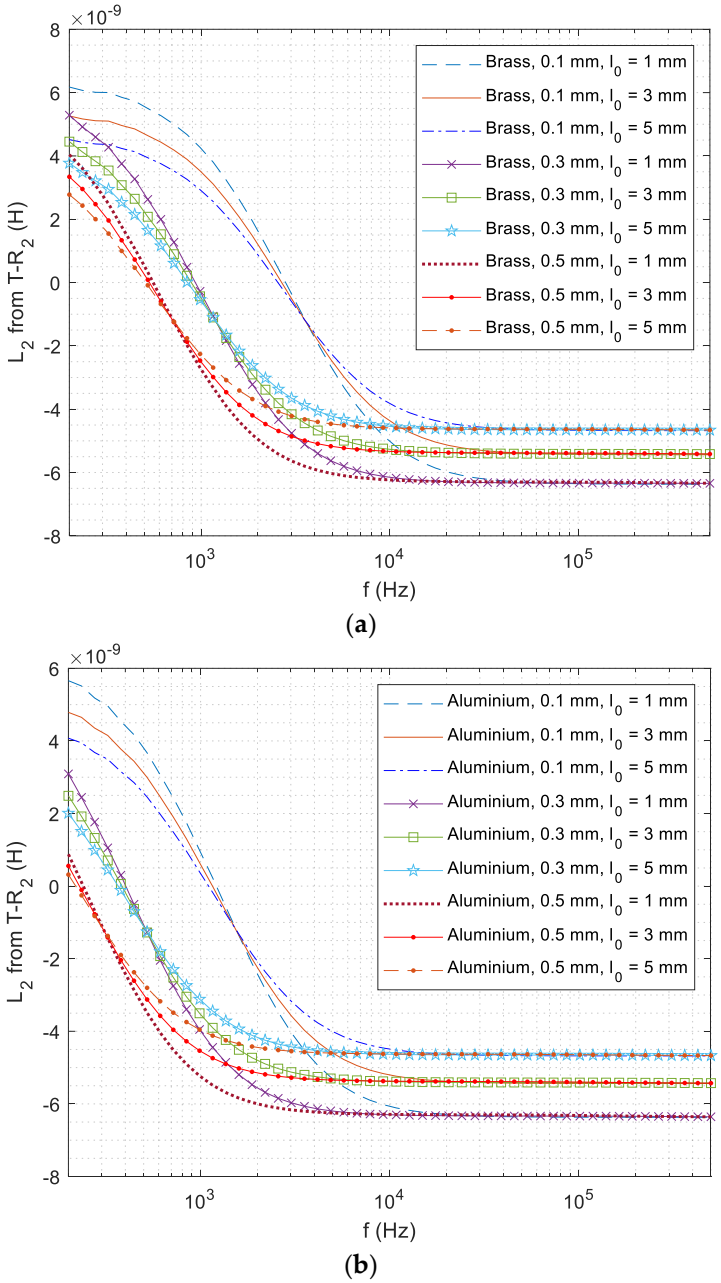

Figure 5. Experimental swept-frequency inductance curves of different lift-off distances for $T-R_2$ above the conductive coating (on DP 1000 steel) with different thicknesses (a) brass (b) aluminium.

Fig. 5 shows the experimental swept-frequency inductance curve from $T-R_2$ sensing pair. Due to the magnetic permeability of ferrous substrate, the inductance curve starts from a positive value instead of zero. With increasing frequency, the inductance crosses zero (zero-crossing frequency feature reported in [48], instead of the point of intersection) and gradually becomes stable especially over 40 kHz, where inductance curves of different coating thicknesses converge. As the overall conductivity of aluminium coatings with DP 1000 substrate is higher than that of brass coatings with DP 1000 substrate, the zero-crossing frequency and whole inductance curve shift left [48]. Moreover, the inductance curve is mainly determined by the lift-off distance between the sensor and test piece for working frequencies over 40 kHz. Considering the effect of other metals, the lift-off distance is retrieved from the inductance under working frequencies over 100 kHz.

Preprints (www.preprints.org) | NOT PEER-REVIEWED | Posted: 8 January 2021 doi:10.20944/preprints202101.0157.v1

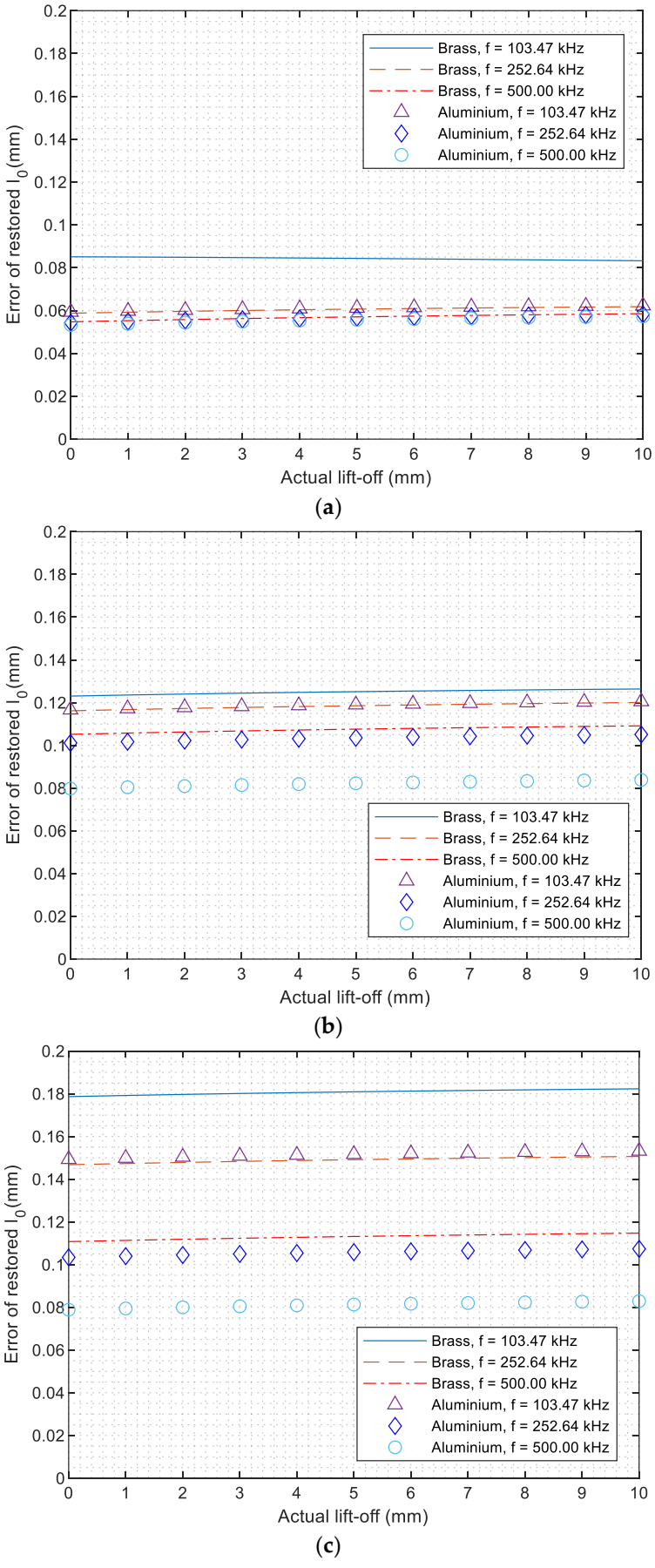

Figure 6. Error of the retrieved lift-off distance for coatings with thickness of (a) 0.1 mm (b) 0.3 mm (c) 0.5 mm.

Preprints (www.preprints.org) | NOT PEER-REVIEWED | Posted: 8 January 2021 doi:10.20944/preprints202101.0157.v1

Fig. 6 shows the error of retrieved lift-off from the measured high-frequency inductance using proposed algorithms (18) and (19). It can be observed that the error of inversed lift-off slightly increases with the actual spacing distance between the sensor and test piece. Overall, the lift-off is slightly overestimated for all the coatings, which is caused by the small deviation of the phase term φ approximation in Fig. 2 (a) and equation (13) and omitting of exponential term $e^{-2\alpha_0 x}$ from (17) to (18). As the change rate of φ for thicker coatings is slightly higher than that of thin coatings, the phase term φ in equation (13) is more underestimated. Consequently, the error of inverse lift-off generally increases with coating thickness. Since the approximation of phase term φ in equation (13) achieves a better performance under higher working frequencies (as Fig. 2 a depicts), the inversed lift-off is more accurate from the inductance under 500 kHz. Therefore, the inverse of coating thickness in the following section is based on the inversed lift-off under 500 kHz. For coatings of different materials and thickness, the error of inversed lift-off has been controlled within 0.2 mm for different coatings thicknesses.

4.2. Effect of high frequency on lift-off retrieval

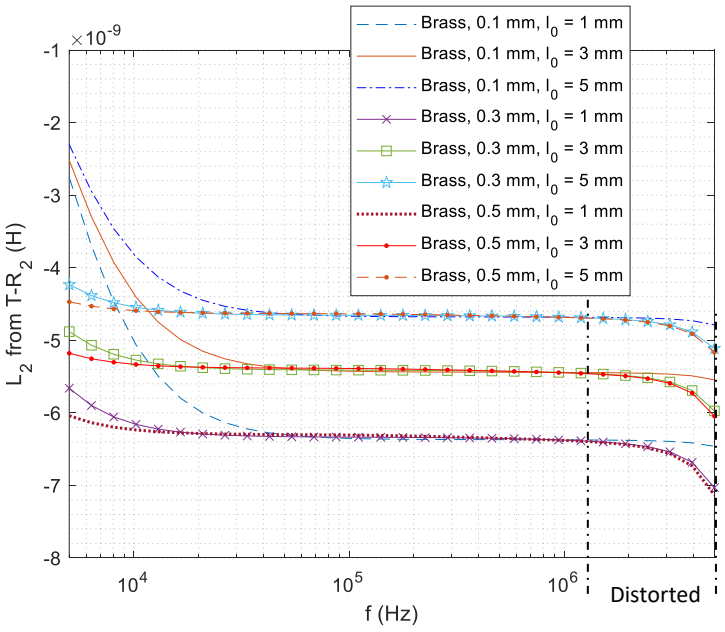

(**a**)

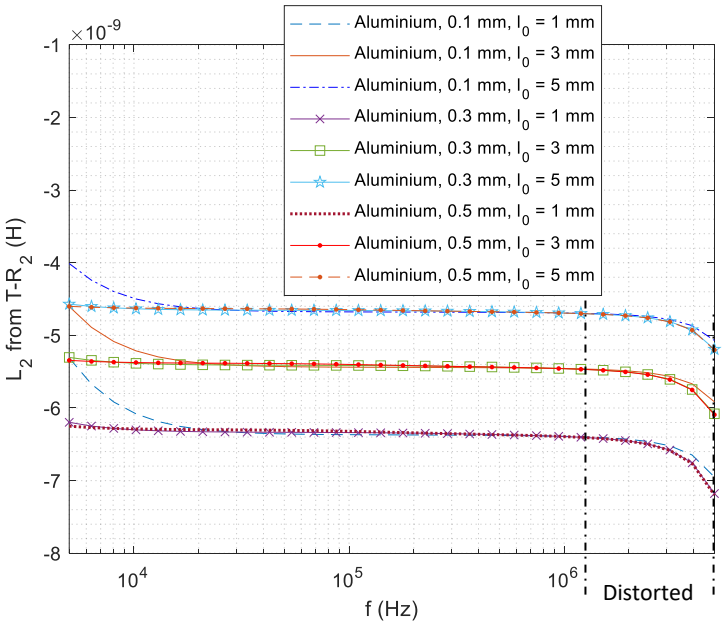

(**b**)

Preprints (www.preprints.org) | NOT PEER-REVIEWED | Posted: 8 January 2021 doi:10.20944/preprints202101.0157.v1

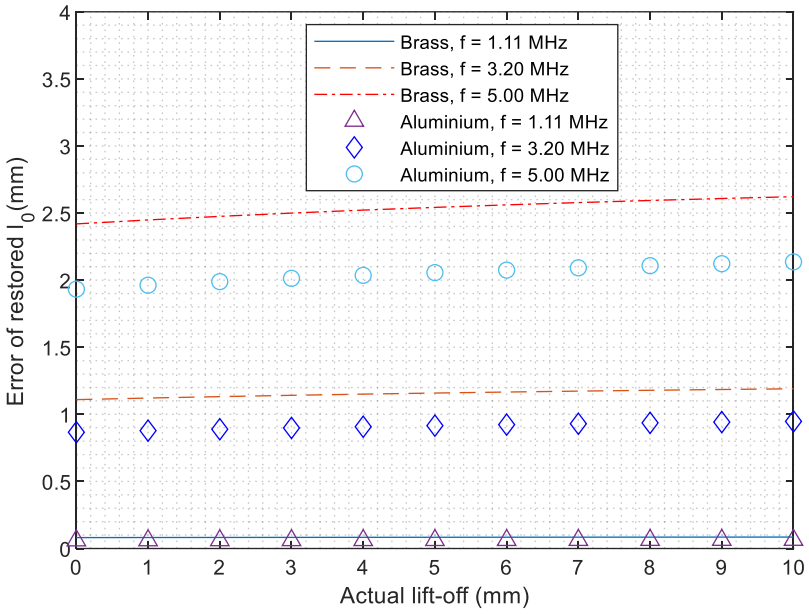

(c)

Figure 7. Distorted swept-frequency inductance (for high working frequencies up to 5 MHz) of different lift-off distances for $T - R_2$ above the conductive coating (on DP 1000 steel) with different thicknesses (a) brass (b) aluminium (c) error of the retrieved lift-off distance for coatings with thickness of 0.3 mm.

Fig. 7 (a) and (b) show the swept-frequency inductance of sensing pair for high working frequencies up to 5 MHz. It can be observed that the inductance curve gradually diverges from the constant value and becomes distorted. Such measurement is caused by various factors, including the resonant/proximity/parasitic effect of coil windings under high frequency (fringe effect of excitation current), and Barkhausen noise effect (where the ferromagnetic domains of the substrate surface are magnetized by the restrained eddy current under the high-frequency skin-effect). Fig. 7 (c) illustrates the error of the retrieved lift-off for coatings with a thickness of 0.3 mm. A higher working frequency (e.g., 5.0 MHz) results in a more distorted inductance and larger error for the lift-off retrieval.

4.3. Retrieval of coating thickness

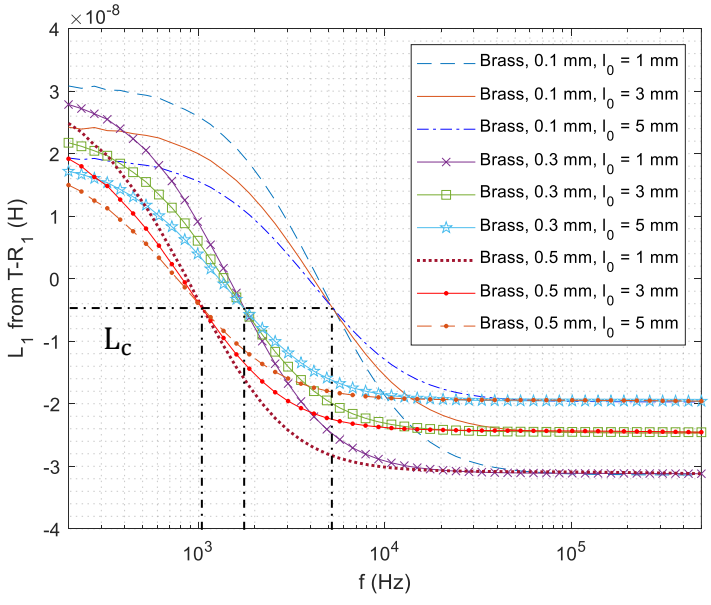

(a)

Preprints (www.preprints.org) | NOT PEER-REVIEWED | Posted: 8 January 2021 doi:10.20944/preprints202101.0157.v1

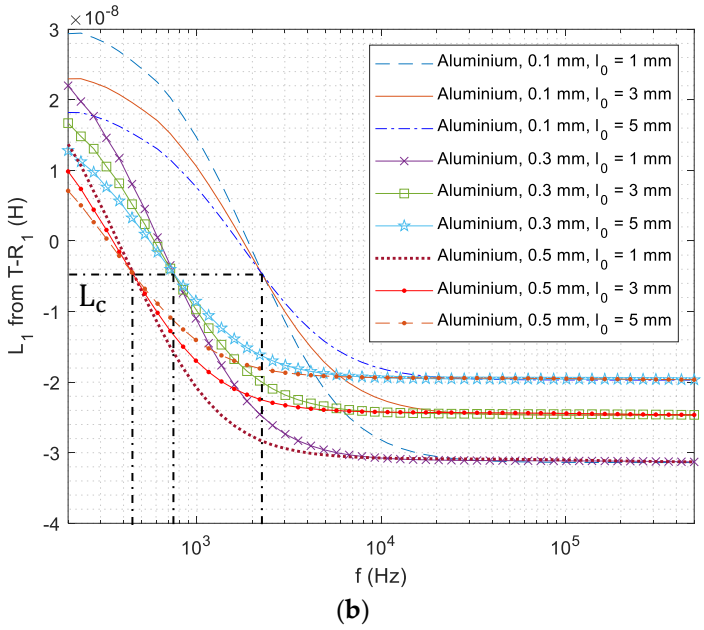

(**b**)

Figure 8. Experimental swept-frequency inductance curves of different lift-off distances for $T-R_1$ above the conductive coating (on DP 1000 steel) with different thicknesses (a) brass (b) aluminium.

Fig. 8 illustrates the measurement of swept-frequency inductance curve from $T-R_1$ sensing pair, which follows a similar trend in Fig. 5. It can be observed that inductance curves of different lift-offs converge at the point (clusters). Moreover, curves of different coating thicknesses and materials share the same LII. Compared to the swept-frequency inductance curve from $T-R_2$ in Fig. 5, the LIF of the lift-off insensitive point and inductance curve slightly shifts towards high frequencies. Since the inductance curve slightly fluctuates under lower frequencies due to the poor SNR, the inverse of coating thickness from the LIF feature achieves a better performance from $T-R_1$ sensing pair (compared to $T-R_2$ sensing pair). Compared to the previous zero-crossing frequency feature [48] where the inductance crosses zero, the LIF is less sensitive to the lift-off variations.

Fig. 9 exhibits corresponded frequencies (LIF) of the LII for different coatings under different lift-offs. It can be observed that LIF slightly fluctuates with increased lift-offs. Moreover, either a highly conductive or thinner coating will render an increased LIF.

Furthermore, parameters including the LIF, inversed lift-off are served as the input for the reconstruction of coating thickness using iterative algorithms from (20) to (22).

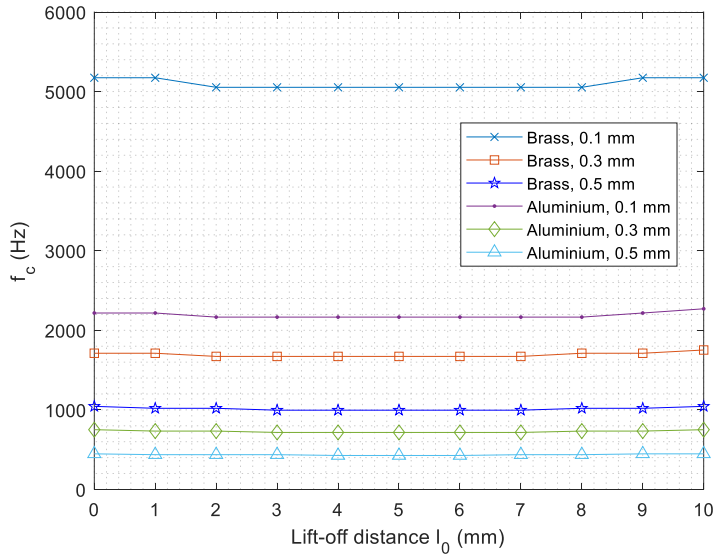

Figure 9. Lift-off insensitive frequency versus lift-off distance for different coatings.

Preprints (www.preprints.org) | NOT PEER-REVIEWED | Posted: 8 January 2021 doi:10.20944/preprints202101.0157.v1

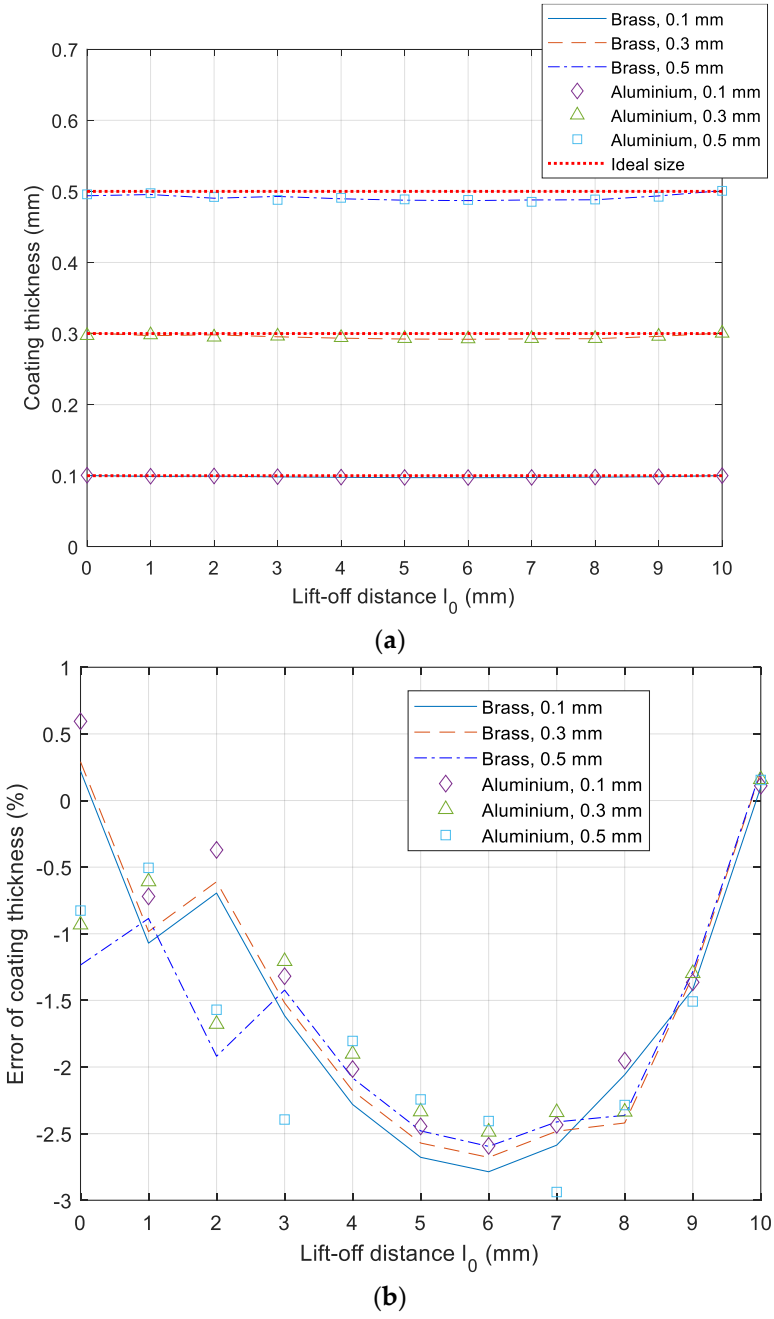

Figure 10. Inverse of coating thickness versus lift-off distance a) absolute value b) error.

In Fig. 10, owing to different inductance sensitivities with respect to different thicknesses, electrical conductivities, and lift-offs [22], the retrieved coating thickness is sensitive to the lift-off variation (compared to inversed lift-off in Fig. 6, and LIF in Fig. 9). As the lift-off increases, the calculated coating thickness drifts away then converges to its actual size. Overall, the inverse error for the thickness of different coatings on the DP 1000 steel is controlled within 3 % for lift-off up to 10 mm.

5. Conclusions

A simplified iterative algorithm is proposed for the computation of the inductance of circular coils above ferrous substrate with non-magnetic coatings under high working frequencies. In this regime, either the phase term or inductance is insensitive to the property of the dual-layer conductors (including the thickness of coatings). The lift-off is retrieved from the high-frequency inductance based on the proposed algorithm. Based on the LII and LIF features, where swept-frequency

inductance curves of different lift-off intersect at one point or converge at point clusters, the thickness of different coatings is calculated in an iterative manner. Considering the sensitivities of inductance with respect to lift-offs and sample parameters, the measurement is based on two different coil-sensing pairs. The sensor consists of two receiving coils (R_1 and R_2) of different lift-offs and one transmitting coil (T) in the middle, with the top sensing pair $T - R_2$ more accurate on the lift-off retrieval and the bottom one $T - R_1$ more sensitive to the sample parameters. Experiments show that the calculation is independent of the lift-off distance variations, with a maximum deviation of 0.18 mm in 10 mm range. Moreover, with the referred LIF and compensated lift-off, the retrieved coating thickness can be controlled within a deviation of 3 %. For different non-magnetic coatings and ferrous substrates, the LII is a constant factor determined by the dimension and geometry of the sensor. The property of non-magnetic coatings (e.g., thickness) and ferrous substrate (e.g., magnetic permeability) effects can thus be retrieved by referring to the corresponding LIF. The proposed method is based on the simplification of inductance algorithms using eddy-current thin-skin effect, which significantly relieved the cumbersome calculations of integrations for the retrieval. Thus, based on the eddy-current thin-skin effect under high frequencies, the proposed formula is used as the embedded algorithm for the online retrieval of lift-offs. Compared to previous techniques of compensating the lift-off error, the lift-off retrieval is directly retrieved from the impedance and used for the retrieval of coating thickness. Moreover, the lift-off range that can be retrieved is extended from 3 mm to 10 mm, while the error of thickness retrieval is still within a deviation of 3 %.

Author Contributions: Conceptualization, X.M.; methodology, X.M. and M.L.; software, X.M. and M.L.; validation, X.M. and M.L.; formal analysis, X.M.; data curation, X.M., M.L., and W.Y.; writing—original draft preparation, X.M.; writing—review and editing, X.M., M.L., and A.B.; supervision, A.B., K.J.K. All authors have read and agreed to the published version of the manuscript.

Conflicts of Interest: The authors declare no conflict of interest.

References

1. Brayden Jr, T. H.; Winters Jr, T. D. Coating thickness measurement system and method of measuring a coating thickness. *U.S. Patent*, **2000**, *No. 6,052,191*.
2. Wang, Y.; et al. Measurement of coating thickness using lift-off point of intersection features from pulsed eddy current signals. *NDT & E International*, **2020**, 116, p. 102333.
3. Zhang, J.; et al. Precision measurement of coating thickness on ferromagnetic tube using pulsed eddy current technique. *International Journal of Precision Engineering and Manufacturing*, **2015**, 16, pp. 1723-1728.
4. Cheng, Y.; et al. Absorbing coating thickness measurement based on lift-off effect of eddy current testing. *International Journal of Applied Electromagnetics and Mechanics*, **2014**, 45, pp. 323-330.
5. Kim, T. O.; et al. Non-contact and in-process measurement of film coating thickness by combining two principles of eddy-current and capacitance sensing. *CIRP annals*, **2007**, 56, pp. 509-512.
6. Tian, Y.; et al. Eddy current based method for coating thickness measurement. *U.S. Patent*, **2016**, *No. 9,377,287*.
7. Yang, H.; Tai, C. Pulsed eddy-current measurement of a conducting coating on a magnetic metal plate. *Measurement science and technology*, **2002**, 13, p.1259.
8. Wang, Z.; Yu, Y. Thickness and Conductivity Measurement of Multilayered Electricity-Conducting Coating by Pulsed Eddy Current Technique: Experimental Investigation. *IEEE Transactions on Instrumentation and Measurement*, **2019**, 68, pp. 3166-3172.
9. Tai, C.; James, H. R.; Moulder, J. C. Thickness and conductivity of metallic layers from pulsed eddy-current measurements. *Review of scientific Instruments*, **1996**, 67, pp. 3965-3972.
10. Kuts, I. V.; et al. Pulsed Eddy Current Non-Destructive Testing of the Coating Thickness. The E-Journal of Nondestructive Testing: XI European Conference on Non-Destructive Testing, Prague, Czech Republic, 2014.
11. He, Y.; et al. Steel corrosion characterization using pulsed eddy current systems. *IEEE Sensors Journal*, **2012**, 12, pp. 2113-2120.
12. Yu, Y.; et al. Quantitative approach for thickness and conductivity measurement of monolayer coating by dual-frequency eddy current technique. *IEEE Transactions on Instrumentation and Measurement*, **2017,** 66, pp. 1874-1882.

13. Antonelli, G.; Ruzzier, M.; Necci, F. Thickness measurement of MCrAlY high-temperature coatings by frequency scanning eddy current technique. *Journal of Engineering for Gas Turbines and Power* ,**1998**, 120, pp. 537-542.
14. Tai, C. Characterization of coatings on magnetic metal using the swept-frequency eddy current method. *Review of Scientific Instruments*, **2000,** 71, pp. 3161-3167.
15. Zhang, D.; et al. Thickness measurement of multi-layer conductive coatings using multifrequency eddy current techniques. *Nondestructive Testing and Evaluation*, **2016**, 31, pp. 191-208.
16. Shamgholi, M.; et al. The Development of Eddy Current Nondestructive Testing Method for Coating Thickness Measurement on the Steel Sheets 4th International Engineering Materials and Metallurgy Conference, Tehran, Iran. 2015.
17. Nix, N. Methods for eliminating error sources of magnetic sensors used for the measurement of coating thickness. *U.S. Patent*, **2004**, No. 6,724,187.
18. Cho, S.; et al. Eddy current brake with a two-layer structure: Calculation and characterization of braking performance. *IEEE Transactions on Magnetics*, **2017**, 53, pp. 1-5.
19. Syas'ko, V. A.; et al., Measurement of electromagnetic parameters of metal-coating thickness measures. *Russian Journal of Nondestructive Testing*, **2018**, 54, pp. 698-710.
20. Li, Y.; et al. Quantitative evaluation of thermal barrier coating based on eddy current technique. *NDT & E International*, **2012**, 50, pp. 29-35.
21. Bavall, L. Determination of coating thickness of a copper-plated steel wire by measurement of the internal wire impedance. *IEEE Transactions on Instrumentation and Measurement*, **1998**, 47, pp.1013-1019.
22. Lu, M.; et al. Determination of the magnetic permeability, electrical conductivity, and thickness of ferrite metallic plates using a multi-frequency electromagnetic sensing system. *IEEE Transactions on Industrial Informatics*, **2019**, 15, pp. 4111-4119.
23. Rodriguez, S.; Xie, Y.; Yin, W.; Peyton., A. J. A FPGA Based Platform for Multi-Frequency Eddy Current Testing. In Proceedings of the 11th European Conference on Non-Destructive Testing (ECNDT 2014), Prague, Czech Republic, pp. 6-10. 2014.
24. Munjal, R.; Sajjad, F.; Wendler, F.; Kanoun, O. Multi-Frequency Inductive Sensor System for Classification of Bi-Metallic Coins. *IEEE Transactions on Instrumentation and Measurement*, **2020**, 70, pp. 1-9. DOI: 10.1109/TIM.2020.3011489
25. Wen, D.; Fan, M.; Cao,B.; Ye, B.; Tian, G. Extraction of LOI Features from Spectral Pulsed Eddy Current Signals for Evaluation of Ferromagnetic Samples. *IEEE Sensors Journal*, **2019**, 19, pp. 189-195.
26. Yin, W.; Peyton, A. J. Thickness measurement of non-magnetic plates using multi-frequency eddy current sensors. *NDT & E International*, **2007**, 40, pp. 43-48.
27. Chen, X.; Lei, Y. Electrical conductivity measurement of ferromagnetic metallic materials using pulsed eddy current method. *NDT & E International*, **2015**, 75, pp. 33-38.
28. Yang, G.; Dib, G.; Udpa, L.; Tamburrino, A.; Udpa, S. S. Rotating Field EC-GMR Sensor for Crack Detection at Fastener Site in Layered Structures. *IEEE Sensors Journal*, **2015**, 15, pp. 463-470.
29. Li, W.; Yuan, X.; Chen, G.; Ge, J.; Yin, X.; Li, K. High sensitivity rotating alternating current field measurement for arbitrary-angle underwater cracks. *NDT&E International*, **2016**, 79, pp. 123-131.
30. Vasic, D.; Bilas, V.; Ambrus, D. Pulsed eddy-current nondestructive testing of ferromagnetic tubes. *IEEE Transactions on Instrumentation and Measurement,* **2004**, 53, pp. 1289-1294.
31. Abidin, I. Z.; Mandache, C.; Tian, G. Y.; Morozov, M. Pulsed eddy current testing with variable duty cycle on rivet joints. *NDT & E International*, **2009**, 42, pp. 599-605.
32. He, Y.; Tian, G.; Zhang, H.; Alamin, M.; Simm, A.; Jackson, P. Steel Corrosion Characterization Using Pulsed Eddy Current Systems. *IEEE Sensors Journal*, **2012**, 12, pp. 2113-2120.
33. Lu, M.; et al. Acceleration of frequency sweeping in eddy-current computation. *IEEE Transactions on Magnetics*, **2017**, 53, pp. 1-8.
34. Shin, Y.; Choi, D.; Kim, Y.; Lee, S. Signal characteristics of differential-pulsed eddy current sensors in the evaluation of plate thickness. *NDT & E International*, **2009**, 42, pp. 215-221.
35. Tian, G. Y.; Sophian, A. Reduction of lift-off effects for pulsed eddy current NDT. *NDT & E International*, **2005**, 38, pp. 319–324.
36. Egorov, A. V.; Polyakov, V. V.; Salita, D. S.; Kolubaev, E. A.; Psakhie, S. G.; Chernyavskii, A. G.; Vorobei, I. V. Inspection of aluminum alloys by a multi-frequency eddy current method. *Defence Technology*, **2015**, 11, pp. 99-103.

37. Zhou, W.; Lu, M.; et al. Three-dimensional electromagnetic mixing models for dual-phase steel microstructures. *Applied Sciences*, **2018**, 8, p. 529.
38. Theodoulidis, T.; Kriezis, E. E. Eddy current canonical problems (with applications to nondestructive evaluation). Henderson, NV, USA: Tech Science Press, 2006, no. 0-9717880-1-4.
39. Tytko, G.; Dziczkowski, L. E-Cored Coil with a Circular Air Gap Inside the Core Column Used in Eddy Current Testing. *IEEE Transactions on Magnetics*, **2015**, 51, pp. 1-4.
40. Yin, W.; Peyton, A. J.; Dickinson, S. J. Simultaneous Measurement of Distance and Thickness of a Thin Metal Plate With an Electromagnetic Sensor Using a Simplified Model. *IEEE Transactions on Instrumentation and Measurement*, **2004**, 53, pp. 1135-1138.
41. Lu, M.; Xu, H.; Zhu, W.; Yin, L.; et al. Conductivity Lift-off Invariance and measurement of permeability for ferrite metallic plates. *NDT & E International*, **2018**, 95, pp. 36-44.
42. Lu, M.; Huang, R.; Yin, W.; Zhao, Q.; Peyton, A. J. Measurement of permeability for ferrous metallic plates using a novel lift-off compensation technique on phase signature. *IEEE Sensors Journal*, **2019**, 19, pp. 7440-7446.
43. Lu, M.; Meng, X.; Yin, W.; Qu, Z.; Wu, F.; et al. Thickness measurement of non-magnetic steel plates using a novel planar triple-coil sensor. *NDT & E International*, **2019**, 107, p. 102148.
44. Huang, R.; Lu, M.; Peyton, A.; Yin, W. Thickness measurement of metallic plates with finite planar dimension using eddy current method. *IEEE Transactions on Instrumentation and Measurement*, **2020**, 69, pp. 8424 – 8431.
45. Lu M.; et al. Measurement of ferromagnetic slabs permeability based on a novel planar triple-coil sensor. *IEEE Sensors Journal*, **2020**, 20, pp. 2904-2910.
46. Avila, J. R. S.; Lu, M.; et al. Accurate measurements of plate thickness with variable lift-off using a combined inductive and capacitive sensor. *NDT & E International*, **2020**, 110, p. 102202.
47. Dodd, C. V.; Deeds, W. E. Analytical solutions to eddy-current probe-coil problems. *Journal of applied physics*, **1968**, 39, pp. 2829-2838.
48. Lu, M.; et al. Reducing the lift-off effect on permeability measurement for magnetic plates from multifrequency induction data. *IEEE Transactions on Instrumentation and Measurement*, **2018**, 67, pp. 167-174.
49. Lu, M.; et al. A novel compensation algorithm for thickness measurement immune to lift-off variations using eddy current method. *IEEE Transactions on Instrumentation and Measurement*, **2016**, 65, pp. 2773-2779.
50. Yin, W.; Tang, J.; Lu, M.; et al. An equivalent-effect phenomenon in eddy current non-destructive testing of thin structures. *IEEE Access*, **2019**, 7, pp. 70296-70307.
51. Chew, W. C. Waves and Fields in Inhomogenous Media. New York, NY, USA: IEEE Press, 1995, chapter. 2, pp. 4–10.
52. Meng, X.; Lu, M.; Yin, W.; Bennecer, A.; Kirk, K. J. Inversion of lift-off distance and thickness for non-magnetic metal using eddy current testing. *IEEE Transactions on Instrumentation and Measurement*, **2020**, 70, pp. 1-8. DOI: 10.1109/TIM.2020.3038289
53. Lu, M.; et al. Determination of Surface Crack Orientation Based on Thin-Skin Regime Using Triple-Coil Drive–Pickup Eddy-Current Sensor. *IEEE Transactions on Instrumentation and Measurement*, **2020**, 70, pp. 1-9. DOI: 10.1109/TIM.2020.3044729
54. W. Yin; et al. Measurements of thickness for metallic plates with co-axial holes using a novel analytical method with the modified integration range. IEEE Access, **2020**, 8. DOI: 10.1109/ACCESS.2020.3035333
55. M. Lu, et al., "Prediction of the asymptotical magnetic polarization tensors for cylindrical samples using the boundary element method," In 2015 IEEE Sensors Applications Symposium (SAS), pp. 1-4. IEEE, 2015.
56. M. Lu et al., "Thickness measurement of metallic film based on a high-frequency feature of triple-coil electromagnetic eddy current sensor," IEEE Transactions on Instrumentation and Measurement, vol. 70, 2020. DOI: 10.1109/TIM.2020.3027929.
57. M. Lu, X. Meng, W. Yin, Z. Qu, F. Wu, J. Tang, et al., "Thickness measurement of non-magnetic steel plates using a novel planar triple-coil sensor," NDT & E International, vol. 107, 2019.
58. M. Lu et al., "Measuring lift-off distance and electromagnetic property of metal using dual-frequency linearity feature," IEEE Transactions on Instrumentation and Measurement, early access, 2020. DOI: 10.1109/TIM.2020.3029348.
59. R. Huang, M. Lu, A. Peyton, and W. Yin, "A novel perturbed matrix inversion based method for the acceleration of finite element analysis in crack-scanning eddy current NDT," IEEE Access, vol. 8, pp. 12438-12444, 2020.

60. M. Lu et al., “Inversion of Distance and Magnetic Permeability Based on Material-Independent and Lift-off Insensitive Algorithms Using Eddy Current Sensor,” IEEE Transactions on Instrumentation and Measurement, vol. 70, 2020. DOI: 10.1109/TIM.2020.3036099.
61. M. Lu et al., “Lift-off tolerant pancake eddy-current sensor for the thickness and spacing measurement of non-magnetic plates,” IEEE Transactions on Instrumentation and Measurement, vol. 70, 2020. DOI: 10.1109/TIM.2020.3033377.
62. R. Huang et al., "Measuring Co-Axial Hole Size of Finite-Size Metallic Disk Based on a Dual-Constraint Integration Feature Using Multi-Frequency Eddy Current Testing," IEEE Transactions on Instrumentation and Measurement, vol. 70, 2020. DOI: 10.1109/TIM.2020.3026762
63. R. Huang et al., "Measurement of the radius of metallic plates based on a novel finite region eigenfunction expansion (FREE) method," IEEE Sensors Journal, vol. 20, 2020. DOI: 10.1109/JSEN.2020.3009443
64. J. Tang et al., "A Novel Efficient FEM Thin Shell Model for Bio-Impedance Analysis," Biosensors, vol. 10, no. 6, pp. 69, 2020.
65. L. Chen, et al., "Textile Based Capacitive Sensor for Physical Rehabilitation via Surface Topological Modification," ACS Nano, vol. 14, no. 7, pp. 8191-8201, 2020. DOI: 10.1021/acsnano.0c01643
66. Z. Jin, et al., "Methods of Controlling Lift-off in Conductivity Invariance Phenomenon for Eddy Current Testing," IEEE ACCESS, vol. 8, pp. 2169-3536, 2020. DOI: 10.1109/ACCESS.2020.3007216.
67. J. Tang, et al., "Effect of frozen-thaw injury on cell membrane and bio-impedance," In 2020 IEEE International Instrumentation and Measurement Technology Conference (I2MTC), pp. 1-6. IEEE, 2020.
68. J. Tang, et al., "Bio-impedance spectroscopy for frozen-thaw of bio-samples: Non-contact inductive measurement and finite element (FE) based cell modelling," Journal of Food Engineering, vol. 272, pp. 109784, 2020.
69. H. Xu et al., "Imaging a weld cross-section using a novel frequency feature in multi-frequency eddy current testing," Insight-Non-Destructive Testing and Condition Monitoring, vol. 61, no. 12, pp. 738 - 743, 2019.
70. Y. Xie et al., "Novel Wearable Sensors for Biomechanical Movement Monitoring Based on Electromagnetic Sensing Techniques," IEEE Sensors Journal, vol. 20, no. 2, 2020. DOI: 10.1109/JSEN.2019.2943487
71. W. Yin et al., "Permeability invariance phenomenon and measurement of electrical conductivity for ferrite metallic plates," Insight-Non-Destructive Testing and Condition Monitoring, vol. 61, no. 8, pp. 472 - 479, 2019.
72. M. Lu et al., "A model for the triboelectric nanogenerator with inductive load and its energy boost potential," Nano Energy, vol. 63, pp. 103883, 2019.
73. M. Lu et al., "Forward solver for deep earth exploration and induction logging using custom built Edge-Element FEM technique," Acta Geologica Sinica, vol. 93, pp. 302-304, 2019.
74. L. Chen et al., "Whole System Design of Wearable Magnetic Induction Sensor for Physical Rehabilitation," Advanced Intelligent Systems, vol. 1, no. 1, pp. 1900037, 2019.
75. Y. X et al., "A self-powered radio frequency (RF) transmission system based on the combination of triboelectric nanogenerator (TENG) and piezoelectric element for disaster rescue/relief," Nano Energy, vol. 54, pp. 331-340, 2018.
76. W. Yin et al., "Custom edge-element FEM solver and its application to eddy-current simulation of realistic 2M-element human brain phantom," Bioelectromagnetics, vol. 39, no. 8, pp. 604-616, 2018.
77. L. Yin et al., "Detection of corrosion pits based on an analytically optimised eddy current sensor," Insight-Non-Destructive Testing and Condition Monitoring, vol. 60, no. 10, pp. 561-567, 2018.
78. W. Yin et al., "Acceleration of eddy current computation for scanning probes," Insight-Non-Destructive Testing and Condition Monitoring, vol. 60, no. 10, pp. 547-555, 2018.
79. W. Zhou et al., "Three-dimensional electromagnetic mixing models for dual-phase steel microstructures," Applied Sciences, vol. 8, no. 4, pp. 547-555, 2018.
80. M. Lu, et al., "Determining the magnetic permeability of ferrite steel strip by a custom inversion method," In Proc. 12th ECNDT, pp. 1-8. 2018.
81. J. Tang, et al., "Cellular structure analysis based on magnetic induction finite element method simulations and measurements," bioRxiv, pp. 275271, 2018. DOI: 10.1101/275271
82. J.R.S. Avila, et al., "A novel dual modality sensor with sensitivities to permittivity, conductivity, and permeability," IEEE Sensors Journal, vol. 18, no. 1, pp. 356-362, 2017.
83. T. Yang, et al., "Level measurement for saline with a small surface area using high frequency electromagnetic sensing technique," Measurement, vol. 101, pp. 118-125, 2017.